

Article

Unraveling the Reaction Mechanism of HCHO Catalytic Oxidation on Pristine Co_3O_4 (110) Surface: A Theoretical Study

Rong Li ^{1,2,3}, Tingting Huang ^{1,2}, Yu Huang ^{1,2,*} , Meijuan Chen ⁴, Shun-cheng Lee ⁵ , Wingkei Ho ⁶ 
and Junji Cao ^{1,2}

¹ State Key Laboratory of Loess and Quaternary Geology (SKLLQG), Key Laboratory of Aerosol Chemistry and Physics, Institute of Earth Environment, Chinese Academy of Sciences, Xi'an 710061, China; lirong@ieecas.cn (R.L.); huangtingtings@163.com (T.H.); cao@loess.llqg.ac.cn (J.C.)

² CAS Center for Excellence in Quaternary Science and Global Change, Xi'an 710061, China

³ University of Chinese Academy of Sciences, Beijing 100049, China

⁴ School of Human Settlements and Civil Engineering, Xi'an Jiaotong University, Xi'an 710049, China; chenmeijuan@mail.xjtu.edu.cn

⁵ Department of Civil and Environmental Engineering, The Hong Kong Polytechnic University, Hong Kong 999077, China; shun-cheng.lee@polyu.edu.hk

⁶ Department of Science and Environmental Studies, The Education University of Hong Kong, Hong Kong 999077, China; keithho@eduhk.hk

* Correspondence: huangyu@ieecas.cn; Tel.: +86-29-6233-6261

Abstract: Various reaction mechanisms for the catalytic degradation of formaldehyde (HCHO) remain to be debated. Density functional theory (DFT) was applied to investigate whether the catalytic oxidation of HCHO on pristine Co_3O_4 (110) surface follows the Mars-van Krevelen (MvK) mechanism or the Langmuir–Hinshelwood (L-H) mechanism. Firstly, HCHO and O_2 co-adsorb on the surface and two H atoms from HCHO are peculiarly prone to transfer to O_2 , forming CO and HOOH. For the MvK mechanism, CO_2 is generated through CO grabbing a lattice oxygen. Meanwhile, the O–O bond of HOOH is broken into two OH groups. One OH fills the oxygen vacancy and its H atom moves to another OH group for H_2O formation. For the L-H mechanism, CO directly obtains one OH group to generate COOH. Subsequently, the H atom of COOH transfers to another OH group along with CO_2 and H_2O generation. Both two mechanisms exhibit a similar maximum activation barrier. The lattice oxygen in the MvK mechanism and the surface-absorbed OH group in the L-H mechanism are the key reactive oxygen species. The small difference in energetic span further suggests that the catalytic cycle through the two mechanisms is feasible. This theoretical study provides new insight into the catalytic reaction path of HCHO oxidation on pristine Co_3O_4 surface.

Keywords: pristine Co_3O_4 ; (110) surface; MvK mechanism; L-H mechanism; density functional theory



Citation: Li, R.; Huang, T.; Huang, Y.; Chen, M.; Lee, S.-c.; Ho, W.; Cao, J. Unraveling the Reaction Mechanism of HCHO Catalytic Oxidation on Pristine Co_3O_4 (110) Surface: A Theoretical Study. *Catalysts* **2022**, *12*, 560. <https://doi.org/10.3390/catal12050560>

Academic Editor: Aleksander Filarowski

Received: 20 April 2022

Accepted: 15 May 2022

Published: 19 May 2022

Publisher's Note: MDPI stays neutral with regard to jurisdictional claims in published maps and institutional affiliations.



Copyright: © 2022 by the authors. Licensee MDPI, Basel, Switzerland. This article is an open access article distributed under the terms and conditions of the Creative Commons Attribution (CC BY) license (<https://creativecommons.org/licenses/by/4.0/>).

1. Introduction

Formaldehyde (HCHO) is one of the most concerning indoor pollutants leading to hazardous effects on human health [1,2], and significant efforts have been made to settle indoor HCHO emissions. Room-temperature catalytic oxidation represents an attractive technology for complete conversion of HCHO to H_2O and CO_2 without the formation of harmful by-products or secondary pollutants, thus making it the most promising HCHO removal technique compared with conventional adsorption and photo-catalytic oxidation [3–7]. Supported noble metals (e.g., Pt [8], Pd [9], Au [10], and Ag [11]) are the most effective catalysts for HCHO catalytic oxidation at room temperature. Nevertheless, the high price and scarcity of noble metals may restrain their wide application in the long term. Transition metal oxides, such as MnO_x [6], Co_3O_4 [12], CeO_2 [13], TiO_2 [14], and their composites [15–17], exhibit comparable catalytic performance and are cost-effective for low temperature HCHO oxidation. Among these catalysts, Co_3O_4 -based catalysts have recently been attractive for low-temperature catalytic applications due to their strong oxidative

capacity, high oxygen redox capability, and facile generation of reactive oxygen species (ROS) [18].

The catalytic path of HCHO oxidation can follow three mechanisms, including the Langmuir–Hinshelwood (L-H) mechanism, Eley–Rideal (E-R) mechanism, and Mars-van Krevelen (MvK) mechanism. Numerous experimental studies proved that the reaction path of HCHO oxidation on Co_3O_4 -based catalysts mainly follows the L-H mechanism [19–22]. These studies utilized oxygen vacancy (O_V) engineering or load noble metals to enhance the catalytic activity of Co_3O_4 -based catalysts at room temperature. Surface-adsorbed ROS obtained by dissociating O_2 from oxygen vacancies or noble metal sites are generally considered to be the most important ROS. For the L-H mechanism, the reaction starts from HCHO and O_2 co-adsorption on surface to form carbonaceous intermediates and ROS, and then the adsorbed carbonaceous intermediates are oxidized by ROS into CO_2 and H_2O . Different from the L-H mechanism, the details of the E-R mechanism are that pre-adsorbed O_2 first forms ROS, which then makes contact with HCHO and further oxidizes it into CO_2 and H_2O . However, the MvK mechanism that the catalytic oxidation of HCHO may follow is usually less frequently mentioned [11]. For the MvK mechanism, lattice oxygen (O_latt) oxidizes HCHO into CO_2 , accompanied by the formation of an oxygen vacancy. Then, adsorbed O_2 dissociates on the oxygen vacancy into two active O atoms, one fills the O vacancy and the other combines with H atoms derived from HCHO for H_2O generation. Thus, the biggest difference between the MvK mechanism and the L-H mechanism is whether surface adsorbed ROS or O_latt participates in HCHO oxidation, yet the possibility that these two routes are jointly involved in the catalytic oxidation of HCHO cannot be ignored.

In order to investigate the catalytic oxidation mechanism of HCHO on the Co_3O_4 surface, the selection of crystal facets with high reactivity is crucial. It is generally believed that increasing the exposure of the (110) surface facilitates the catalytic oxidation of various gaseous pollutants on Co_3O_4 [23–25], since the Co_3O_4 (110) surface possesses a large amount of Co^{3+} active sites, which can efficiently chemisorb reactants. Ma et al. indicated that mesoporous 2D- Co_3O_4 exhibited preferable HCHO oxidation activity compared to Co_3O_4 nanosheets, which can be explained by the dominance of the Co^{3+} -rich (110) surface in 2D- Co_3O_4 [19]. Similarly, Bai et al. compared nano- Co_3O_4 , 2D- Co_3O_4 , and 3D- Co_3O_4 catalysts and found that the high HCHO oxidation activity of 3D- Co_3O_4 was attributed to greater (110) surface exposure [12]. The theoretical study by Deng et al. suggested that the catalytic oxidation of HCHO followed the MvK mechanism on the perfect Co_3O_4 (110) surface, while on the Co_3O_4 (110) surface with oxygen vacancies it followed the L-H mechanism [26]. However, whether the HCHO oxidation on the pristine Co_3O_4 (110) surface follows the L-H mechanism remains to be further explored.

Herein, this work focuses on comparing the MvK mechanism and L-H mechanism of HCHO oxidation on the pristine Co_3O_4 (110) surface through density functional theory (DFT). The activation barriers, reaction energy, and maximum energetic span (δE) of elementary reactions for possible reaction paths have been examined. The results help to broaden the fundamental understanding of reaction mechanisms of HCHO oxidation over Co_3O_4 -based catalysts.

2. Results and Discussion

2.1. Possible Adsorption Species

According to the experimental studies of the HCHO oxidation over Co_3O_4 -based catalysts, a complete catalytic oxidation process is usually accompanied by the formation of intermediates such as CH_2O_2 , HCOOH , and HCOO [17,19,27]. These intermediates are gradually oxidized by ROS (including O, OH,) and finally generate CO_2 and H_2O [20,28,29]. Therefore, there indeed exists different kinds of possible species in the reaction of HCHO oxidation to CO_2 and H_2O . In order to explore the reaction mechanism in detail, the (110)-B termination was chosen to model the Co_3O_4 surface (the reasons for choosing (110)-B

termination are detailed in Section 3.1). The $p(2 \times \sqrt{3})$ supercell slabs were utilized for the Co_3O_4 (110)-B surface, which are visualized in Figure 1.

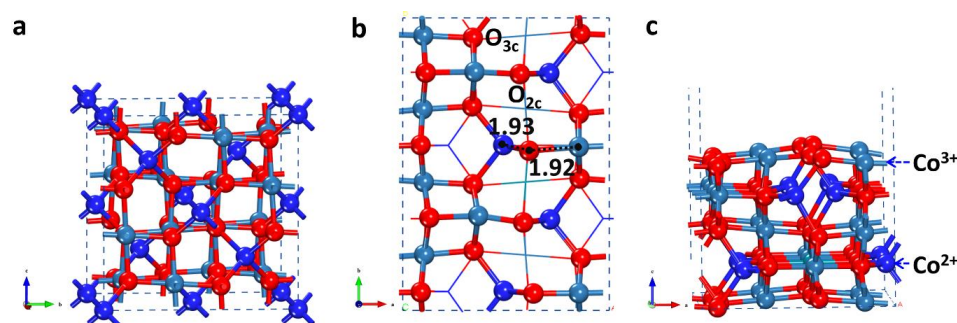


Figure 1. (a) Bulk Co_3O_4 , (b) top view and (c) side view of Co_3O_4 (110)-B surface. Co^{3+} , Co^{2+} , and O atoms are shown in light blue, dark blue, and red, respectively. In addition, in the top view of structures, the atoms at the top and sub layers are illustrated in ball-and-stick model, and the rest are in line model. These illustrations are utilized throughout this paper. The unit of bond lengths are Å.

The location of all possible intermediates on the Co_3O_4 (110) surface should be confirmed. The most stable adsorption configurations of HCHO and O_2 have been given in Figure 2. In addition, Figure 3 presents the adsorption configurations of possible intermediates. The corresponding adsorption energies and key structural parameters are listed in Table 1.

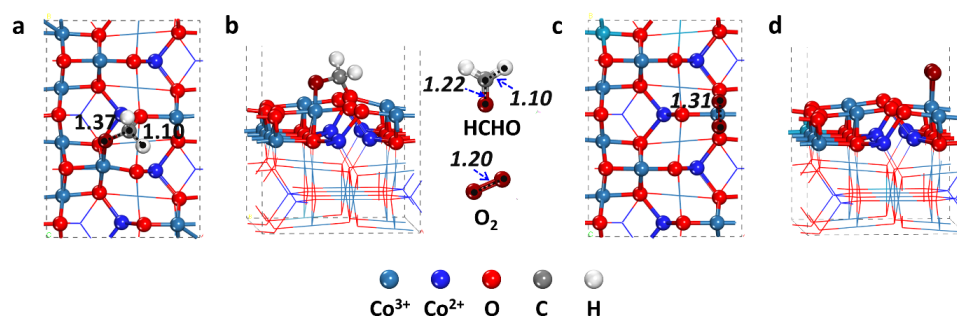


Figure 2. The most stable adsorption configurations together with electron density difference of HCHO (a,b) and O_2 (c,d) on the Co_3O_4 (110) surface. The unit of bond lengths are Å.

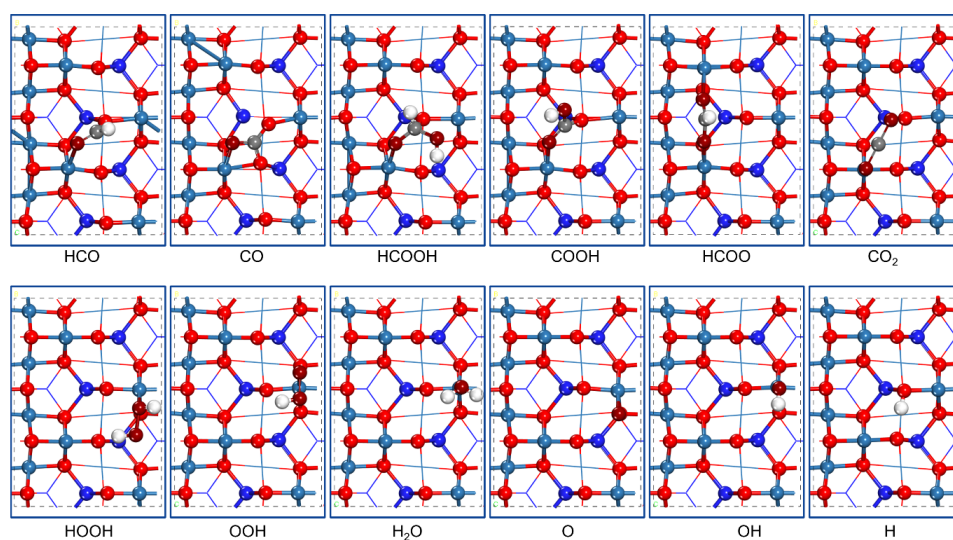


Figure 3. The most stable adsorption configurations of possible intermediate species involved in HCHO oxidation to CO_2 and H_2O on Co_3O_4 (110) surface.

Table 1. Adsorption energies and key structural parameters of the stable configurations for the possible adsorbed species involved in HCHO oxidation to CO₂ and H₂O on Co₃O₄ (110) surface.

Species	E_{ads} (eV)	Adsorption/Configuration	Distance (Å)	Bonding Details	
				Bond	Length (Å)
HCHO	1.28	C-O _{2c} , O-Co ³⁺	1.467, 1.898	C-O	1.372
HCO	3.45	C-O _{2c} , O-Co ³⁺	1.315, 2.222	C-O	1.250
CO	3.57	C-two O _{2c}	1.281, 1.349	C-O	1.283
HCOOH	0.76	C-O _{2c} , O-Co ³⁺	1.455, 1.969	C-O	1.355
COOH	3.71	C-O _{2c} , O-Co ³⁺	1.303, 2.025	C-O/C-O	1.260/1.355
HCOO	2.23	O-Co ²⁺ , O-Co ²⁺	2.006, 2.104	C-O/C-O	1.260/1.279
CO ₂	0.01	away from the surface	—	C-O	1.181
HOOH	1.13	O-Co ³⁺	2.077	O-O	1.483
OOH	1.26	O-Co ³⁺	1.909	O-O	1.455
O ₂	0.85	O-Co ³⁺	1.930, 1.937	O-O	1.310
H ₂ O	0.74	O-Co ³⁺	2.140	O-H	0.979
OH	2.35	O-Co ³⁺	1.849	O-H	0.979
O	2.87	O-Co ³⁺	1.750	—	—
H	3.74	H-O _{2c}	1.002	—	—

HCHO, HCO, CO HCHO and HCO both adsorb on the surface by C atom bonding to the O_{2c} site and O atom bonding to the Co³⁺ site, and their adsorption energies are 1.28 and 3.45 eV, respectively. CO adsorbs on the surface via the C atom located on the middle of two O_{2c} atoms and the O atom bonded to a Co³⁺ site with the adsorption energy of 3.57 eV.

HCOOH, COOH, HCOO, CO₂ HCOOH and COOH adsorb on the surface via C atom connecting to the O_{2c} site and the O atom connecting to Co³⁺ site, and their adsorption energies are 0.76 and 3.71 eV, respectively. HCOO adsorbs on surface with two O atoms connecting to two Co³⁺ sites with the adsorption energy of 2.23 eV. CO₂ weakly adsorbs on the surface by O atom bonding to the Co³⁺ site with the adsorption energy of 0.01 eV.

HOOH, OOH, O₂ HOOH, OOH, and O₂ are all located on the surface via O atom bonding to Co³⁺ site, and their adsorption energies are 1.13, 1.26, and 0.85 eV, respectively.

H₂O, OH, O, H H₂O, OH, and O adsorb on the surface via O atom connecting to Co³⁺ site, and their adsorption energies are 0.74, 2.35, and 2.87 eV, respectively. H atom connects to O_{2c} with an adsorption energy of 3.74 eV.

To better understand the desorption behavior of the obtained product CO₂ and H₂O molecules at ambient conditions, the desorption time (τ) is implemented [30], which is expressed in Section 3.1. The calculated desorption time for CO₂ and H₂O molecules at ambient temperature are 1.14×10^{-3} and 1.76 s, respectively, indicating that CO₂ and H₂O molecules are physical adsorbed. Therefore, they can desorb easily from the Co₃O₄ surface, which facilitates the complete catalytic reaction.

2.2. Reactions Starting from HCHO and O₂ Co-Adsorbing on Co₃O₄ (110) Surface

From the result of the absorption calculation, the adsorption energies of HCHO and O₂ are 1.28 eV and 0.85 eV, respectively, suggesting that HCHO presents stronger adsorption capability than O₂ on Co₃O₄ (110) surface. While for the co-adsorption configuration (Figure 4), HCHO and O₂ locate on two different sites and maintain a distance of 2.35 Å. Therefore, HCHO and O₂ can co-adsorb on Co₃O₄ (110) surface without rejection. The O–O bond length of the adsorbed O₂ molecule is elongated to 1.29 Å, which is longer than that of free O₂ (1.23 Å) and similar to O₂ adsorption individually (1.31 Å). Based on the Mulliken analysis, the O atom as an intermediate has similar atomic charges to the individual adsorbed O₂ molecule, which further confirms the strong chemical adsorption.

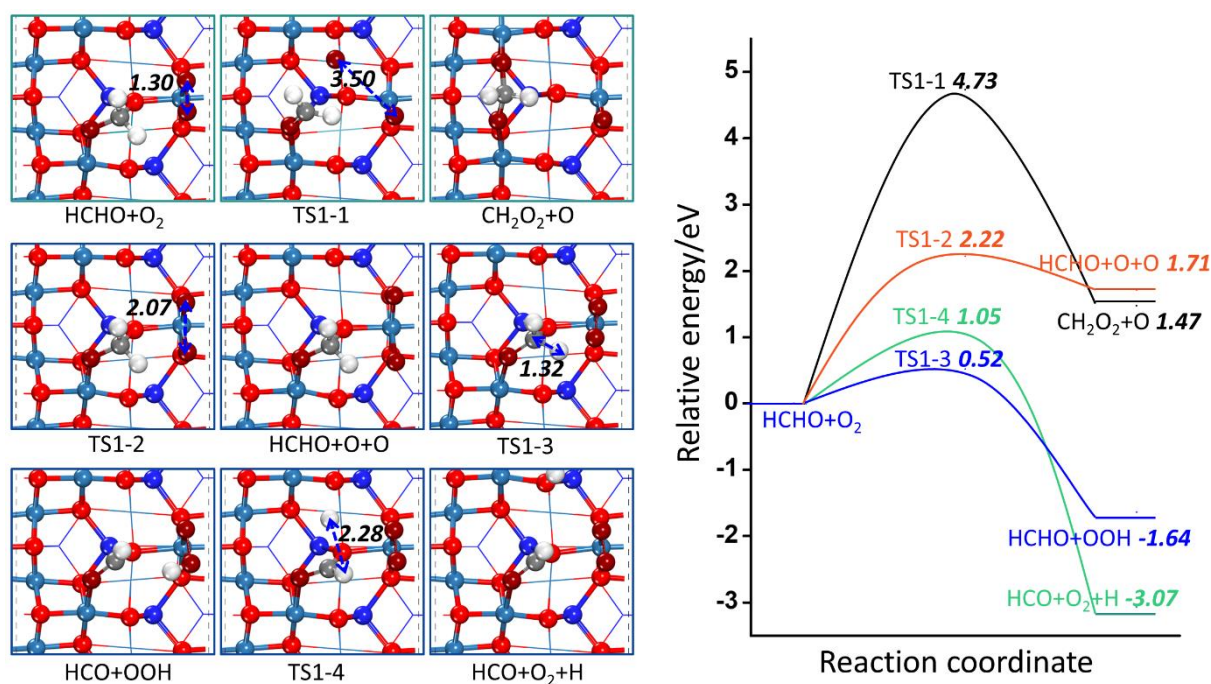


Figure 4. The potential energy profile of the first step of HCHO oxidation together with the structures of TSs and FSs on Co_3O_4 (110) surface. The unit of bond lengths are Å.

We first considered the E-R mechanism on the Co_3O_4 (110) surface. The first elementary reaction is the contact of O_2 with HCHO to form CH_2O_2 and an O atom. If gaseous O_2 is contacted with HCHO pre-adsorbed on the surface, there will be no conversion into CH_2O_2 and O due to the lack of a transition state. Whereas, if HCHO in the gaseous phase is contacted with surface pre-adsorbed O_2 , it will convert into CH_2O_2 and an O atom. However, the activation energy can reach as high as 5.51 eV. Therefore, the E-R mechanism was excluded from consideration. Subsequently, the L-H mechanism and MvK mechanism were investigated in detail. From the co-adsorption of HCHO and O_2 on the Co_3O_4 (110) surface to the CO_2 and H_2O production, HCHO would lose two H atoms and gain one O atom for the formation of CO_2 . Meanwhile, O_2 would lose one O atom and gain two H atoms for the formation of H_2O . Based on these two mechanisms, the corresponding activation barriers and reaction energy of all possible elementary reactions involved in HCHO oxidation have been listed in Table 2.

2.2.1. The Possible First Step of HCHO Oxidation

According to Table 2, all reactions on Co_3O_4 (110) surface are represented by $\text{R}_n\text{-m}$ ($n = 1\sim 5$; $m = 1\sim 10$). The reactions from R1-1 to R1-4 represent four possible initial steps when HCHO and O_2 co-adsorb on Co_3O_4 (110) surface. Figure 4 presents the potential energy profiles of possible pathways of the four possible initial steps together with transition states (TSs) and final states (FSs) on the Co_3O_4 (110) surface.

R1-1 goes through TS1-1 to form CH_2O_2 and O. Firstly, HCHO adsorbs at hollow site, and O_2 adsorbs on the top Co^{3+} site with the O–O bond length of 1.31 Å. Then, one O atom tends to get close to the C atom of HCHO with the O–O distance extending to 3.50 Å. In the final state, the O=O distance is lengthened to 4.69 Å and becomes broken, forming CH_2O_2 with two O atoms connecting on two Co^{3+} sites, and the remaining O atom is adsorbed on another Co^{3+} site. The activation barrier and reaction energy of this elementary reaction are 4.73 eV and 1.47 eV, respectively. For R1-2, O_2 can dissociate into two O atoms through TS1-2, where the O–O distance is elongated to 2.07 Å. In the final state, the O–O distance is lengthened to 2.76 Å and broken, forming two O atoms co-adsorbed on the Co^{3+} site. The activation barrier and reaction energy of this elementary reaction are 2.22 eV and 1.71 eV, respectively. R1-3 and R1-4 are reactions of HCHO dissociation into HCO and H atom,

and the difference is whether the H atom adsorbs on the Co_3O_4 (110) surface or combines with O_2 to generate OOH. In TS1-3, one H atom of HCHO tends to combine with O_2 to form OOH with the C-H bond elongating to 1.32 Å and O-H bond shortening to 1.61 Å. In the final state, HCO adsorbs on the hollow site and OOH adsorbs on the Co^{3+} site. The activation barrier and reaction energy of this elementary reaction are 0.52 eV and -1.64 eV, respectively. In TS1-4, the C-H distance is elongated to 2.29 Å from 1.11 Å of the adsorbed HCHO. In the final state, HCO adsorbs on the hollow site with the H atom adsorbing on the Co^{3+} site. The activation barrier and reaction energy are 1.05 eV and -3.07 eV, respectively.

Table 2. All possible elementary reactions with the corresponding activation barriers (E_a /eV) and reaction energies (ΔE /eV) involved in HCHO oxidation on Co_3O_4 (110) surface.

	Reactions	Co_3O_4 (110) Surface	
		E_a /eV	ΔE /eV
R1-1	$\text{HCHO} + \text{O}_2 \rightarrow \text{CH}_2\text{O}_2 + \text{O}$	4.73	1.47
R1-2	$\text{HCHO} + \text{O}_2 \rightarrow \text{HCHO} + \text{O} + \text{O}$	2.22	1.71
R1-3	$\text{HCHO} + \text{O}_2 \rightarrow \text{HCO} + \text{OOH}$	0.52	-1.64
R1-4	$\text{HCHO} + \text{O}_2 \rightarrow \text{HCO} + \text{H} + \text{O}_2$	1.05	-3.07
	$\text{HCO} + \text{O}_{\text{latt}} + \text{OOH} \rightarrow \text{HCOO} + \text{O}_{\text{V}} + \text{OOH}$	-	0.16
R2-1	$\text{HCOO} + \text{O}_{\text{V}} + \text{OOH} \rightarrow \text{HCOO} + \text{OH} + \text{O}_{\text{latt}}$	1.25	-0.60
R2-2	$\text{HCOO} + \text{OH} \rightarrow \text{CO}_2 + \text{H} + \text{OH}$	2.24	-2.55
R2-3	$\text{CO}_2 + \text{H} + \text{OH} \rightarrow \text{CO}_2 + \text{H}_2\text{O}$	1.09	0.48
R3-1	$\text{HCO} + \text{OOH} \rightarrow \text{CO} + \text{H} + \text{OOH}$	4.26	-2.78
R3-2	$\text{CO} + \text{O}_{\text{latt}} + \text{H} + \text{OOH} \rightarrow \text{CO}_2 + \text{O}_{\text{V}} + \text{H} + \text{OOH}$	2.02	1.59
R3-3	$\text{CO}_2 + \text{O}_{\text{V}} + \text{H} + \text{OOH} \rightarrow \text{CO}_2 + \text{OH} + \text{H} + \text{O}_{\text{latt}}$	1.16	-1.77
R3-4	$\text{CO}_2 + \text{H} + \text{OH} \rightarrow \text{CO}_2 + \text{H}_2\text{O}$	1.40	0.48
R3-5	$\text{CO} + \text{O}_{\text{latt}} + \text{H} + \text{OOH} \rightarrow \text{COOH} + \text{O}_{\text{V}} + \text{OOH}$	5.36	1.84
R3-6	$\text{COOH} + \text{O}_{\text{V}} + \text{OOH} \rightarrow \text{COOH} + \text{OH} + \text{O}_{\text{latt}}$	1.80	-2.39
R3-7	$\text{COOH} + \text{OOH} \rightarrow \text{CO}_2 + \text{H}_2\text{O}$	1.24	0.84
R3-8	$\text{HCO} + \text{OOH} \rightarrow \text{CO} + \text{HOOH}$	1.62	-1.70
R3-9	$\text{CO} + \text{O}_{\text{latt}} + \text{HOOH} \rightarrow \text{CO}_2 + \text{O}_{\text{V}} + \text{HOOH}$	1.85	0.86
R3-10	$\text{CO}_2 + \text{O}_{\text{V}} + \text{HOOH} \rightarrow \text{CO}_2 + \text{O}_{\text{latt}} + \text{H} + \text{OH}$	1.00	-2.12
R4-1	$\text{HCO} + \text{OOH} \rightarrow \text{HCO} + \text{O} + \text{OH}$	0.68	0.21
R4-2	$\text{HCO} + \text{O} + \text{OH} \rightarrow \text{HCOO} + \text{OH}$	4.05	-0.65
R4-3	$\text{HCOO} + \text{OH} \rightarrow \text{CO}_2 + \text{H} + \text{OH}$	2.24	-2.55
R4-4	$\text{CO}_2 + \text{H} + \text{OH} \rightarrow \text{CO}_2 + \text{H}_2\text{O}$	1.09	0.48
R4-5	$\text{HCO} + \text{O} + \text{OH} \rightarrow \text{HCOOH} + \text{O}$	1.11	0.04
R4-6	$\text{HCOOH} + \text{O} \rightarrow \text{HCOO} + \text{H} + \text{O}$	2.05	-0.84
R4-7	$\text{HCOO} + \text{H} + \text{O} \rightarrow \text{HCOO} + \text{OH}$	0.76	0.16
R4-8	$\text{HCOO} + \text{OH} \rightarrow \text{CO}_2 + \text{H} + \text{OH}$	2.24	-2.55
R5-1	$\text{HCO} + \text{OOH} \rightarrow \text{CO} + \text{H} + \text{OOH}$	0.98	0.37
R5-2	$\text{CO} + \text{H} + \text{OOH} \rightarrow \text{CO} + \text{H} + \text{O} + \text{OH}$	4.26	-2.78
R5-3	$\text{CO} + \text{H} + \text{O} + \text{OH} \rightarrow \text{CO}_2 + \text{OH} + \text{H}$	6.20	-0.55
R5-4	$\text{CO}_2 + \text{OH} + \text{H} \rightarrow \text{CO}_2 + \text{H}_2\text{O}$	1.09	0.48
R5-5	$\text{CO} + \text{H} + \text{O} + \text{OH} \rightarrow \text{COOH} + \text{O} + \text{H}$	2.30	0.12
R5-6	$\text{COOH} + \text{O} + \text{H} \rightarrow \text{CO}_2 + \text{H} + \text{OH}$	4.68	-0.67
R5-7	$\text{HCO} + \text{OOH} \rightarrow \text{CO} + \text{HOOH}$	1.62	-1.70
R5-8	$\text{CO} + \text{HOOH} \rightarrow \text{COOH} + \text{OH}$	0.52	-1.63
R5-9	$\text{COOH} + \text{OH} \rightarrow \text{CO}_2 + \text{H}_2\text{O}$	1.24	0.84

The case where HCHO obtains the O_{latt} for CH_2O_2 formation is also considered. However, the formed CH_2O_2 still adsorbs with the O atom filling the (O_{V}), and the configuration is no different with HCHO adsorbing on the pristine surface similar to the final state of R1-1, thus this reaction is not considered. Through comparing the activation barrier and reaction energy, it is found that R1-3 of HCO and OOH formation is the most favorable reaction with the absolutely low activation barrier. Moreover, R1-3 is exothermic, indicating this step is not only thermodynamically but also kinetically favored. It is worth mentioning

that although R1-4 is the most exothermic, its activation barrier is much higher than that of R1-3, which is kinetically hindered. Thus, the first step of HCHO reacting with O₂ is in favor of forming HCO and OOH on the Co₃O₄ (110) surface, and the subsequent pathway of HCHO oxidation is considered starting from HCO and OOH.

In order to investigate why O₂ comfortably accepts one H atom for OOH formation, the PDOS and charge density difference is displayed in Figure 5. The energy levels of Co minority α -spin d orbitals and O₂ π^* orbitals are well matched, leading to partial occupation of the formed d- π^* orbitals. While the strong spin polarization provides large exchange stabilization energy for the majority β -spin orbitals, resulting in Co β -spin d-orbitals with energy levels about 1.0 eV lower than the π^* orbitals of O₂. Therefore, no conspicuous interaction of β orbitals is observed, indicating that only the α π^* orbitals of O₂ are partially occupied, which forces O₂ to be of a radical nature, and active for hydrogenation. When O₂ is hydrogenated to OOH, one electron transfers from the H atom to the β π^* orbitals of O₂, and both α and β DOS of Co 3d orbitals overlap with OOH's π^* orbitals, which further weakens the O–O bond. Therefore, the enhanced interaction and larger occupation of the π^* orbitals in OOH leads to a lower O–O bond order, which is responsible for the lower dissociation barrier than that for O₂.

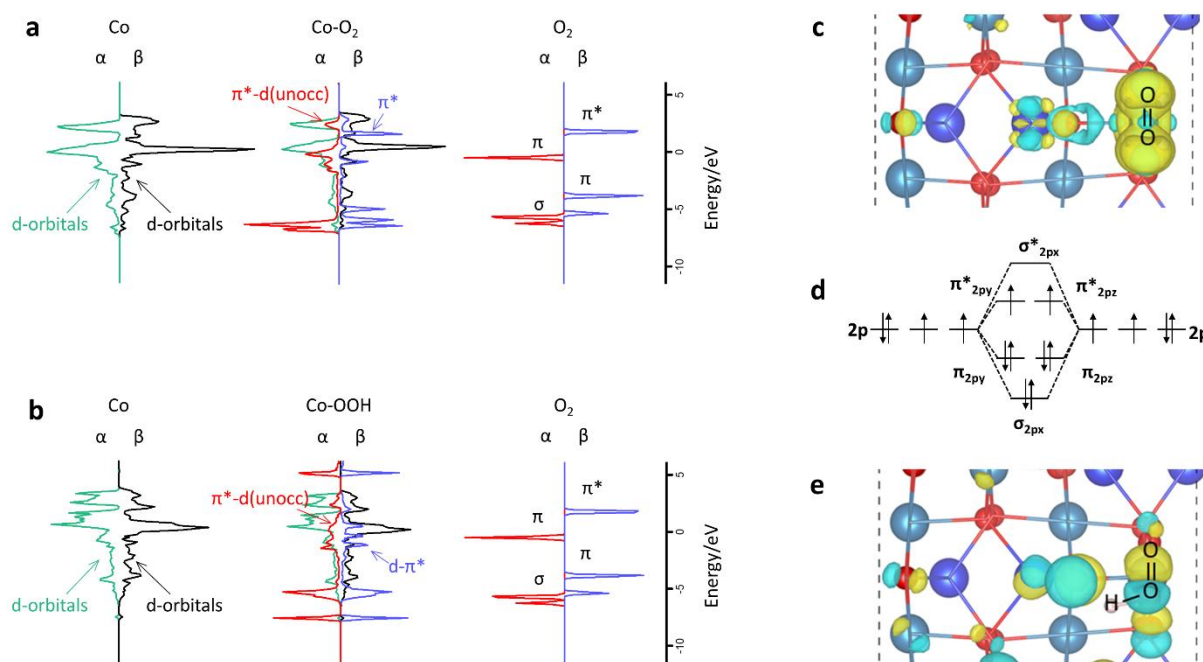


Figure 5. Electronic structure analysis. (a) Projected electronic density of states (PDOS) and schematic illustrations of 3D orbitals of Co on Co₃O₄ (110) surface, 2p-orbitals of the O₂ gas molecule, and their interaction within Co₃O₄-O₂ configuration. (b) PDOS and schematic illustrations for Co₃O₄-OOH interaction configuration. As the O₂ and OOH adsorb on a Co top site, the PDOS displays this Co atom and O₂/OOH. (c,e) The charge density difference of O₂ and OOH adsorb on Co₃O₄ (110) surface, respectively. (d) O₂ molecular orbitals.

2.2.2. HCHO Catalytic Oxidation Mechanism on Co₃O₄ (110) Surface from HCO and OOH MvK Mechanism

The corresponding elementary reactions are revealed in Table 2, where the reactions related to MvK mechanism are marked R2-n and R3-n. The adsorbed HCO can react with O_{latt} to generate HCOO and O_v, followed by the OOH dissociation into OH and an O atom, and O atom filling O_v to restore the surface (R2-1). Subsequently, CO₂ is formed by OH oxidation through C-H breaking away from HCOO (R2-2), and H atom migration to OH to produce H₂O (R2-3). Another alternative reaction path is described below: HCO first dehydrogenates into CO (R3-1), which can pick up O_{latt} to form CO₂ and

O_V (R3-2). Then, OOH is dissociated into OH and an O atom, which fills O_V to restore O_{latt} (R3-3). Meanwhile, OH combines with H atom to form H_2O (R3-4). In addition, O_{latt} can also adsorb H atom from HCO dehydrogenation to form COOH (R3-5), which is further oxidized to CO_2 and H_2O by OOH, accompanied by the recovery of O_V to O_{latt} (R3-5 and R3-7). It is worth mentioning that the H atom of HCO can also transfer to OOH for CO and HOOH formation (R3-8). Then, CO can be oxidized by O_{latt} (R3-9), and the formed O_V can be restored by an O atom produced from the HOOH decomposition, accompanied by the formation of H_2O (R3-10). Therefore, four possible routes account for the MvK mechanism.

The potential energy profile and possible reaction paths of TSs and FSs on Co_3O_4 (110) surface are shown in Figures 6 and 7. The difference in line color indicates different paths. As shown in Figure 6, after HCO and OOH co-adsorption, HCO is more favorable for connecting to O_{latt} to form HCOO than dissociating into CO and H atom, because the dissociation barrier of 4.26 eV is much higher than that of HCOO formation with almost no activation barrier. Even so, the CO path is still considered, because concerning the catalytic cycles, one transition state does not determine the kinetics. The determining states are not necessarily the highest transition state and the lowest intermediate state. The condition that TOF-determining transition state (TDTS) and the TOF-determining intermediate (TDI) must maximize the energetic span, thus the determining states may be different from the extreme state of the energy profile. After HCOO formation via the oxidation of O_{latt} , the following oxygen vacancy filling, dehydrogenation and OH combining with H atom for H_2O generation go through TS2-1, TS2-2 and TS2-3, and their activation barriers are 1.25 eV, 2.24 eV and 1.09 eV, respectively. For the paths of CO capturing O_{latt} or OH shown in Figure 7, the H atom of HCO first transfers to surface (R3-1) or OOH (R3-8) with the activation barrier of 4.26 eV and 1.62 eV, respectively, indicating that H atom preferentially bonds to OOH rather than surface.

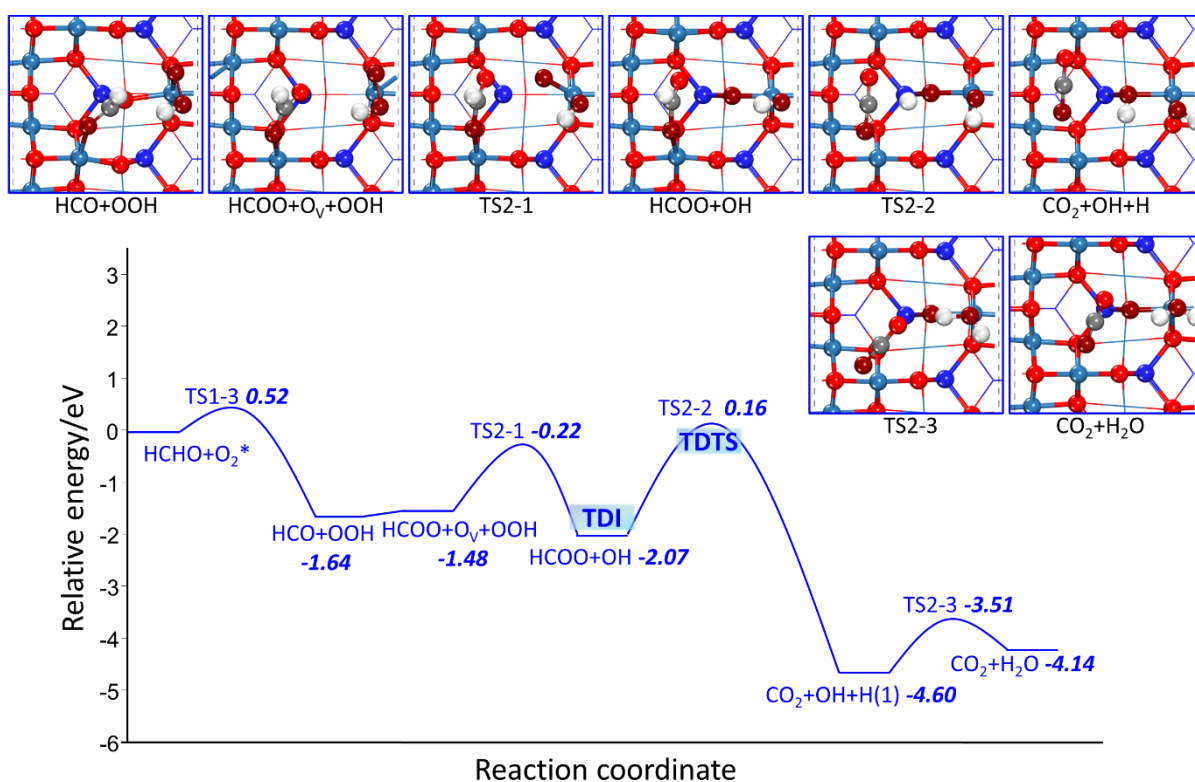


Figure 6. The potential energy profile of HCHO oxidation based on MvK mechanism through HCO grabbing O_{latt} together with the structures of TSs and FSs on Co_3O_4 (110) surface.

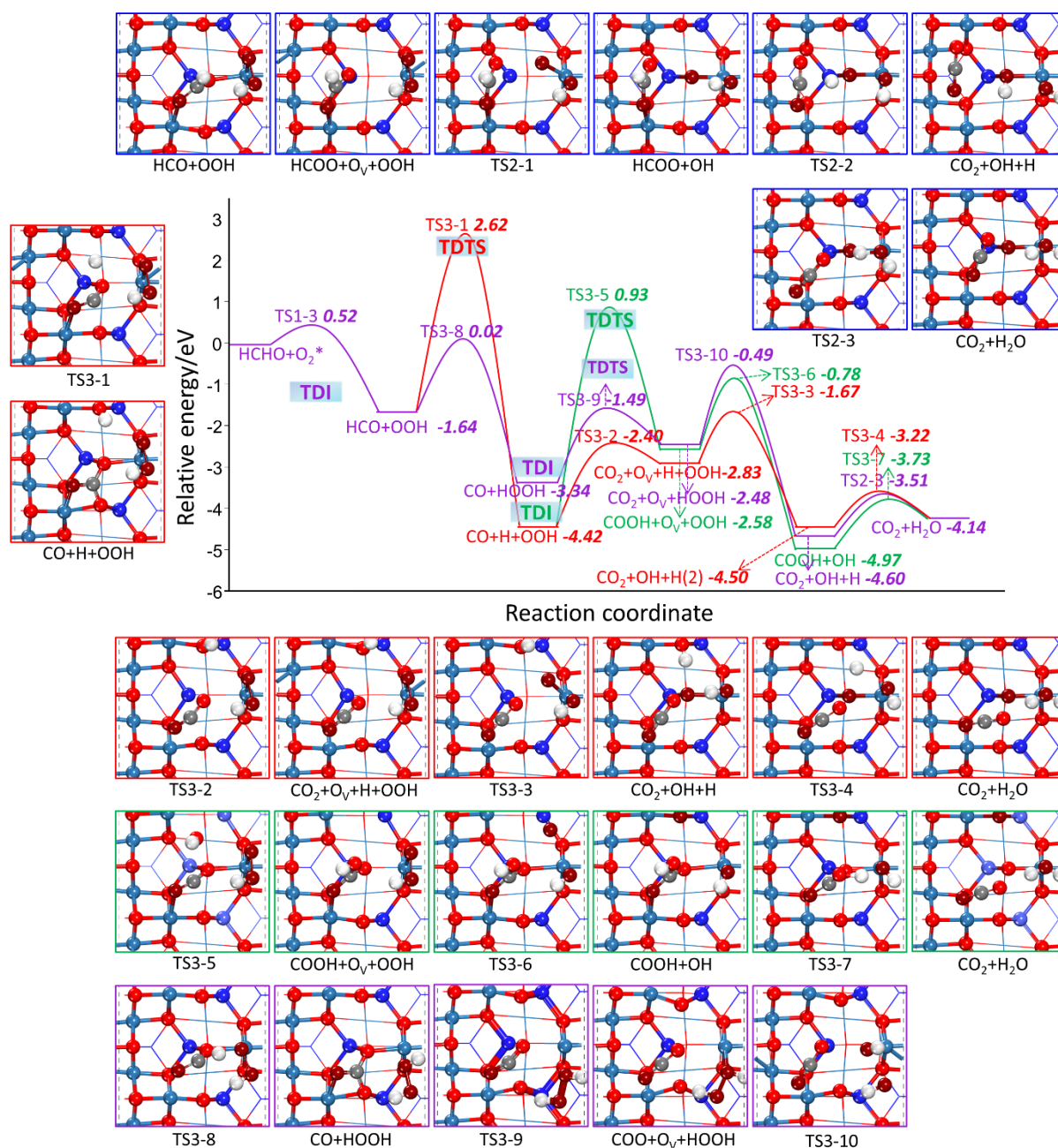


Figure 7. The potential energy profile of HCHO oxidation based on MvK mechanism through CO grabbing O_{latt} together with the structures of TSs and FSs on Co_3O_4 (110) surface.

Starting from the reaction of $\text{CO} + \text{H} + \text{OOH}$ (R3-2, R3-5), CO binds to O_{latt} for CO_2 formation through TS3-2 and binds to lattice OH for COOH formation through TS3-5 with the activation barrier of 2.02 eV and 5.36 eV, respectively. The two reaction steps are endothermic with reaction energies of 1.59 and 1.84 eV, respectively, suggesting the combination of CO with lattice OH for COOH formation is blocked kinetically and thermodynamically. The following O_{V} filling by OOH dissociation through TS3-3 and TS3-6 exhibits the activation barrier of 1.16 eV and 1.80 eV, respectively, which are different from that of R2-1, indicating that OOH dissociation is affected by co-adsorbents. As for the reaction of OH combining with H atom (TS3-4) and the reaction of H atom of COOH transferring to OH for H_2O formation (TS3-7), their activation barriers are 1.40 eV and 1.24 eV, respectively. Starting from the reaction of $\text{CO} + \text{HOOH}$, CO reacts with O_{latt} to produce CO_2 , and HOOH dissociates into two OH groups. One OH occupies O_{V} , the other

OH reacts with H atom to produce H₂O. The activation barrier for these three elementary reactions (R3-9, R3-10, R2-3) are 1.85, 1.00, and 1.09 eV, respectively. Through comparing the four reaction paths, the purple line in Figure 7 is the most preferable as the maximum activation barrier of 1.85 eV is much lower than other three paths with the maximum barrier of 4.26 eV.

As for the catalytic cycles, the TDTS for blue, red, green and purple line marked reaction paths are TS2-2, TS3-1, TS3-5, and TS3-9, respectively. Their corresponding TDI are HCOO + OH, HCOO + O_v + OOH, CO + H + OOH and CO + HOOH, respectively. As the TDTS comes after the TDI, according to formula (5a), the δE for these four reaction routes are 2.24 eV, 4.26 eV, 5.36 eV, and 1.85 eV, respectively, which means that the efficiency of the catalytic cycles of the purple line marked reaction path are satisfactory. In short, irrespective of whether considering single route or catalytic cycles, the specific reaction paths representing the MvK mechanism are described below: firstly, two H atoms of HCHO continuously transfer to O₂, forming CO and HOOH. Then, CO grabs O_{latt} to generate CO₂, and HOOH dissociates into two OH groups with one of them occupying O_v, and its H atom moves to another OH for H₂O formation.

L-H Mechanism

The difference between the L-H mechanism and the MvK mechanism is that the ROS binding to carbon intermediates are derived from surface adsorbed oxygen species, rather than O_{latt}. The specific reactions related to the L-H mechanism are marked R4-n and R5-n in Table 2. Starting from HCO and OOH absorbed on Co₃O₄ (110) surface, the O–O bond of OOH dissociates into OH and O atom (R4-1), which can bind to HCO for HCOO (R4-2) or HCOOH formation (R4-5). HCOO can be oxidized by OH to produce CO₂ and H₂O (R4-3 and R4-4); whereas HCOOH combines with O atom to form HCOO and OH (R4-6 and R4-7), which in turn react to produce CO₂ and H₂O (R4-8). In addition, HCO can be dehydrogenated to form CO (R5-1). The O–O bond of OOH decomposes into O atom and an OH group (R5-2), the former combines with CO to form CO₂ (R5-3) and the latter combines with H atom to form H₂O (R5-4). Moreover, OH can also combine with CO to form COOH, which is subsequently converted into CO₂ (R5-5 and R5-6). The H atom from HCO dehydrogenation can bind to OOH for HOOH formation (R5-7). It reacts with CO to form COOH and OH (R5-8), which are finally converted to CO₂ and H₂O (R5-9). Therefore, five possible routes account for the L-H mechanism.

The potential energy profile and possible reaction pathways of TSs and FSs on the Co₃O₄ (110) surface are shown in Figures 8 and 9. As shown in Figure 8, HCO follows the L-H mechanism to grab surface adsorbed oxygen species via two reaction paths. After HCO and OOH co-adsorption, O–O bond of OOH is broken to form an O atom and OH adsorbed on Co³⁺ site through TS4-1. The dissociation barrier is 0.68 eV and the reaction energy is 0.21 eV. In TS4-2, an O atom approaches HCO, and the C–O bond length is shortened from 3.36 Å to 1.98 Å; In TS4-5, OH rotates and moves to HCO, and the C–O distance is shortened from 3.13 Å to 2.11 Å. The activation barrier of the two transition states are 4.05 eV and 1.11 eV, respectively, and the reaction energies are –0.65 eV and 0.04 eV, respectively, indicating that the combination of HCO to OH is kinetically feasible. This is against that of the MvK mechanism, in which HCO preferentially combines with O_{latt}, suggesting that the lattice oxygen species and adsorbed oxygen species possess different electronic properties that affect their reaction capability. In addition, for transition states (TS4-6, TS4-7, and TS4-8) through which HCOOH is converted to CO₂ and H₂O, their energy barriers are lower than those through HCOO paths (TS4-3 and TS4-4), indicating that the route starting from HCO combining with OH is preferable.

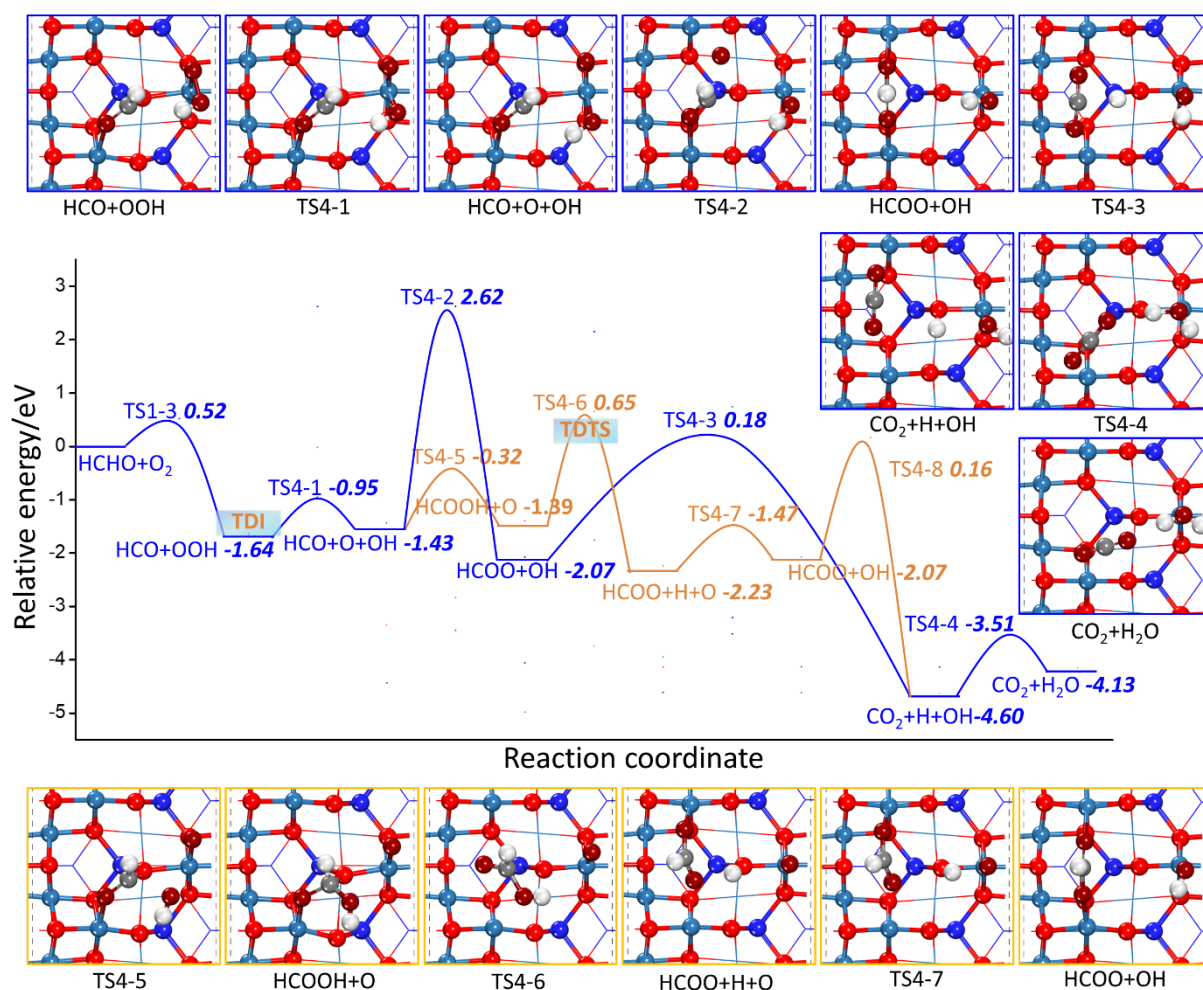


Figure 8. The potential energy profile of HCHO oxidation based on the L-H mechanism through HCO grabbing the surface adsorbed oxygen species together with the structures of TSs and FSs on Co_3O_4 (110) surface.

As revealed in Figure 9, another three possible reaction paths start with the dehydrogenation of adsorbed HCO to form CO, which further follows the L-H mechanism to grab surface adsorbed oxygen species. The H atom generated by the dehydrogenation of HCO can be combined with lattice oxygen through TS5-1, whose activation barrier and reaction energy are 4.26 eV and 2.78 eV, respectively. The H atom can also be combined with OOH through TS5-7 to form HOOH, whose activation barrier and reaction energy are 1.62 eV and -1.70 eV, respectively. In this reaction, the C-H distance is elongated to 1.49 Å along with the H-O distance shortened to 1.28 Å. Therefore, it can be inferred that H atom preferentially bonds with OOH rather than other locations on the surface after cleaving away from HCO. Starting from the reaction of CO + H + OOH, the O-O bond of OOH ruptures again through TS5-2, whose activation barrier and reaction energy are 0.98 eV and 0.37 eV, respectively. CO can react with O atom to form CO₂ via TS5-3 or OH to form COOH via TS5-5. Their activation barriers are 6.20 eV and 2.30 eV, respectively, and their reaction energies are -0.55 eV and 0.12 eV, respectively. This suggests that the CO reaction with OH is more preferable than O atom, which is consistent with the HCO reaction with OH or O, further indicating that surface adsorbed OH is an important ROS. The following COOH dehydrogenation by O atom via TS5-6 may be prevented by the high activation barrier of 4.68 eV. Starting from the reaction of CO+HOOH, CO can directly capture OH from HOOH for COOH formation via TS5-8 with the activation barrier as low as 0.52 eV. Meanwhile, the O-O distance is elongated 2.28 Å and C-O distance is shortened to 2.24 Å. This reaction step is also kinetically favored with reaction energy of -1.63 eV. The H atom

of COOH can transfer to OH through TS5-9 with the activation barrier and reaction energy of 1.24 and 0.84 eV, respectively. Comparing to R5-6 with dehydrogenation of COOH with the H atom adsorbed on the O atom, H atom prefers to be close to OH, which is similar to the fact that the H atom of HCO preferentially reacts directly with the OOH rather than bond with the surface adsorbed O atom. In conclusion, among five reaction paths, the light blue line marked route in Figure 9 is the most favorable, because the maximum energy barrier is much lower than that of other four paths.

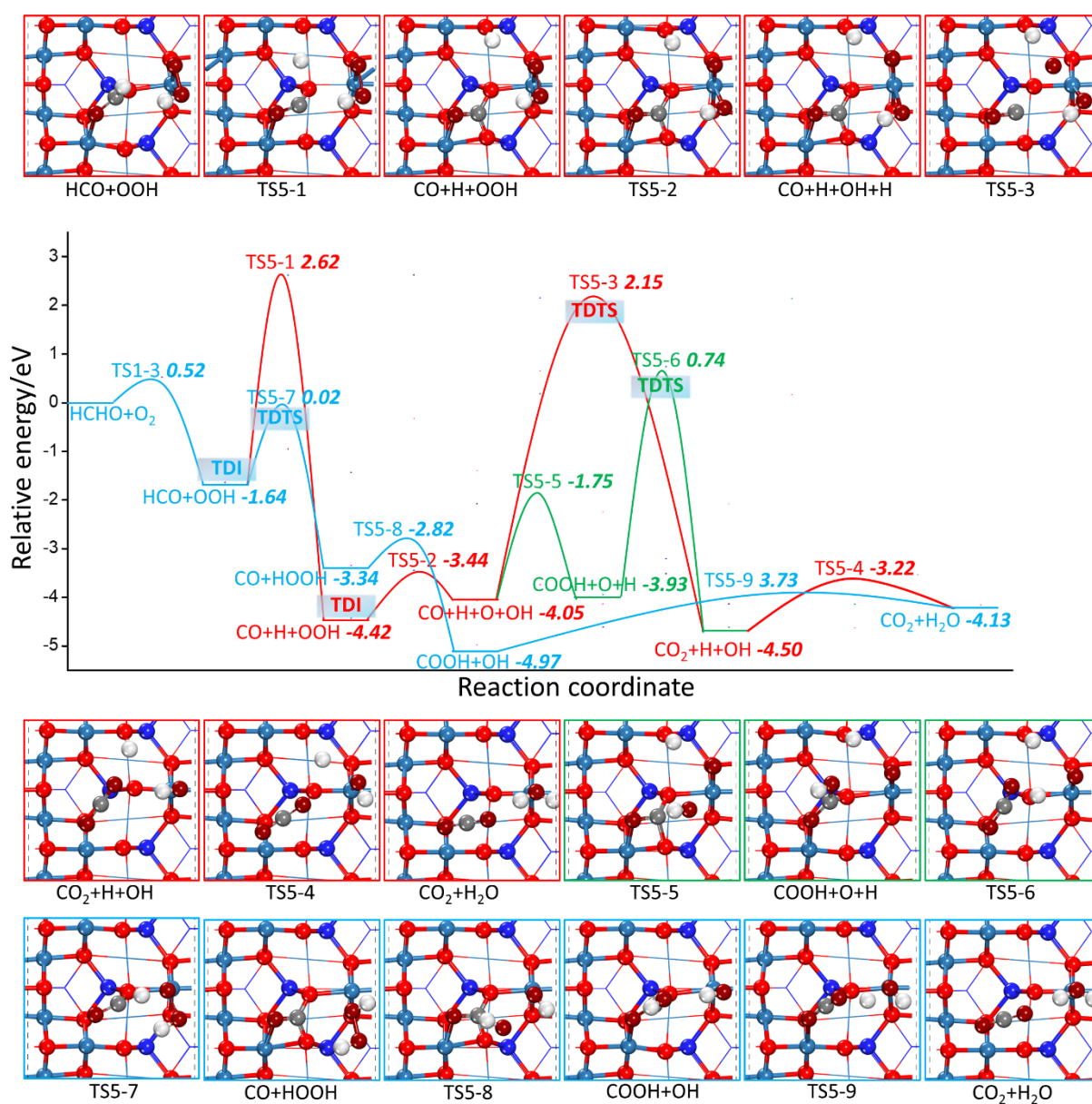


Figure 9. The potential energy profile of HCHO oxidation based on the L-H mechanism through CO grabbing the surface adsorbed oxygen species together with the structures of TSs and FSs on Co_3O_4 (110) surface.

In Figures 8 and 9, the TDTS and TDI marked in different colors represent different paths of TDTS and TDI. As the TDTS comes after the TDI for the five routes, according to formula (5a), the δE for these five routes are 4.26 eV, 2.29 eV, 6.57 eV, 5.16 eV, and 1.65 eV, respectively, which means that the efficiency of catalytic cycles of the light blue line marked path is satisfactory. Therefore, the optimal reaction path of the HCHO oxidation process is as follows: two H atoms of HCHO are successively transferred directly to O₂ to form

HOOH. Subsequently, the O–O bond of HOOH is broken to generate two OH. One OH binds to CO to form COOH, whose H atom further combines with another OH to finally generate CO₂ and H₂O.

2.2.3. Comparison of HCHO Catalytic Oxidation through MvK and L-H Mechanism

Starting from HCHO and O₂ co-adsorption, the most favorable reaction paths that belong to MvK and L-H mechanism are shown in Figure 10 and Scheme 1. Two H atoms of HCHO transfer to O₂ continuously for CO and HOOH formation are the first two favorable steps. For MvK mechanism, CO grabs O_{1latt} to generate CO₂ firstly. The maximum activation barrier is 1.85 eV in this reaction path. The subsequent steps are the O–O bond of HOOH breaking and O vacancy filling by O atom of OH. Finally, H atom move to another OH for H₂O formation. For L-H mechanism, COOH is formed through CO drawing OH from HOOH, and then H atom of COOH is taken away by another OH for CO₂ and H₂O formation. The maximum activation barrier of this reaction path is 1.65 eV, corresponding to the second H atom of HCHO dehydrogenation, which is slightly lower than that of MvK mechanism. Therefore, the highest energy barriers to overcome for the MvK and L-H mechanisms are similar, making both mechanisms feasible. The δE of the two paths correspond exactly to the activation barrier, suggesting that the catalytic cycle through the two mechanisms are equivalent to some extent. It is worth noting that due to the relatively strong exotherm of the reaction, HCHO cannot be oxidized smoothly at room temperature if the energy released in the previous cycles cannot be fully utilized for subsequent cycles. In addition, the maximum δE cannot be affected by the reaction energy according to formula (5b), resulting in TDTS appearing after TDI in all possible paths through MvK and L-H mechanism.

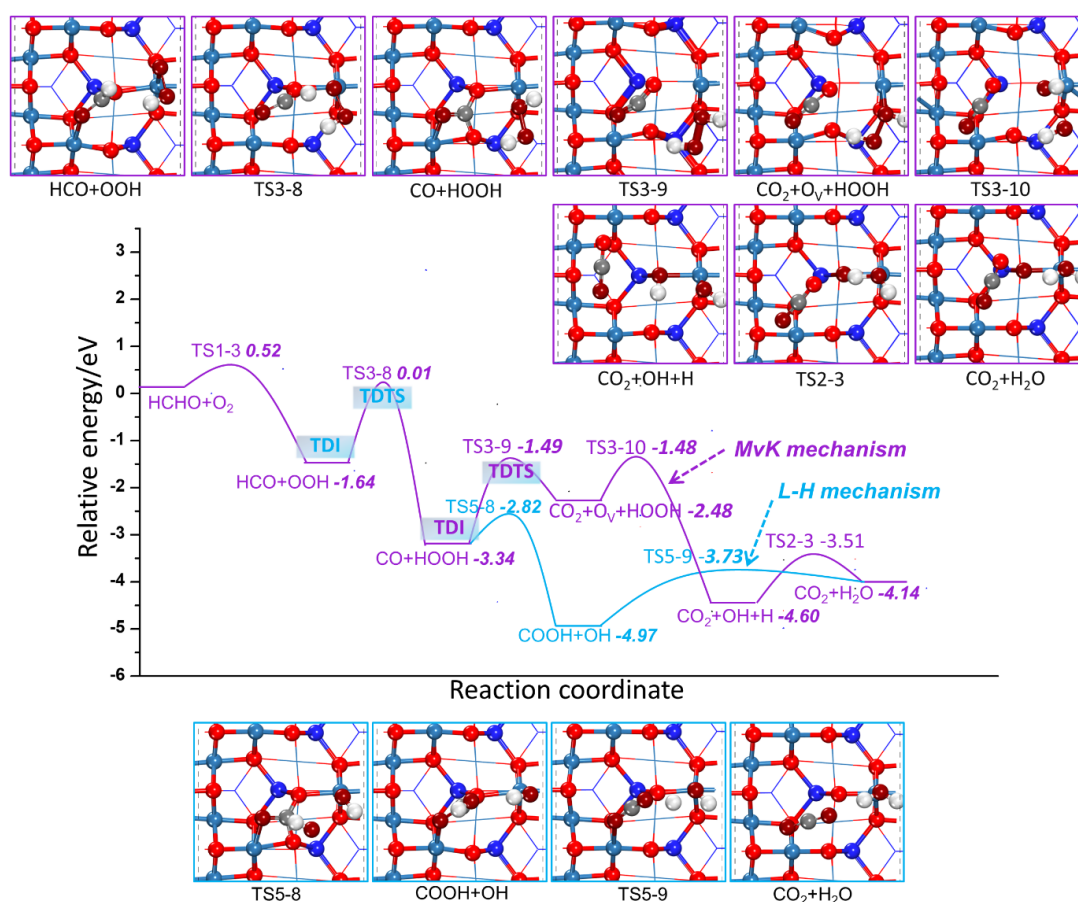
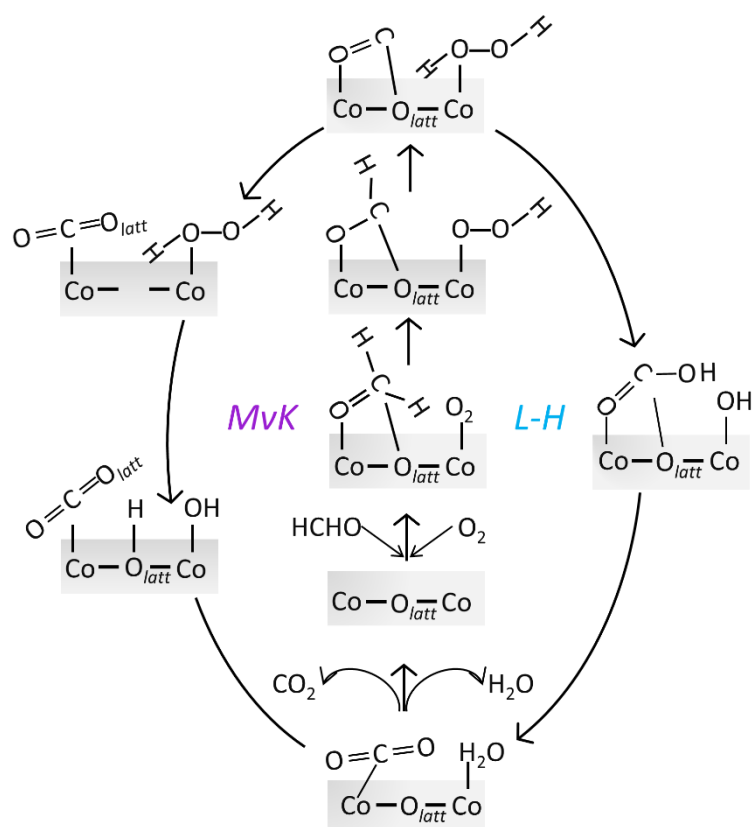


Figure 10. Potential energy diagram for the most favorable pathways of HCHO catalytic oxidation through the MvK and L-H mechanism.



Scheme 1. Elementary reaction steps of HCHO catalytic oxidation based on MvK and L-H mechanism on Co_3O_4 (110) surface.

3. Computational Details

3.1. Surface Models

Co_3O_4 has a spinel structure (Fd3m) which contains half-filled octahedral sites with Co^{3+} cations and tetrahedral sites with Co^{2+} cations. For the Co_3O_4 (110) surface, it bears two different terminations, usually denoted as the A and B terminations: the (110)-A termination exposes two types of cations (Co^{2+} and Co^{3+}) and one type of anion (three-fold coordinated O_{3c}), whereas the (110)-B termination has only one type of cation (Co^{3+}) and two types of anions (two-fold coordinated O_{2c} and three-fold coordinated O_{3c}). Chen et al. [31] have reported the curves of Gibbs surface energy of these two terminations against oxygen chemical potential and found that the terminal B surface possessed a lower Gibbs surface energy in oxygen-rich conditions. Considering the oxygen chemical potential under the common work conditions of HCHO oxidation ($P_{\text{O}_2}/P_0 = 0.2$; $T = 300\text{--}330\text{ K}$), the (110)-B termination was energetically more stable than the (110)-A termination. Therefore, the (110)-B termination was chosen to model the catalyst surface. We simulated symmetric slabs with an odd number of five layers, for which the total dipole moment was zero. This slab was stoichiometric and symmetric along the surface normal plane. The $p(2 \times \sqrt{3})$ supercell slabs were utilized for Co_3O_4 (110)-B surface, which can be seen in Figure 1. The bottom two Co-O layers are fixed. Whereas the topmost three Co-O layers and the adsorbates are fully relaxed in all calculations.

3.2. Computational Details

All the calculations were performed in the framework of the density functional theory (DFT) by using the Cambridge Sequential Total Energy Package (CASTEP) in Material Studio 8.0 of Accelrys. The generalized gradient approximation (GGA) was chosen to represent the exchange-correlation potential in the formulation of the Perdew–Burke–Ernzerhof (PBE) [32]. Owing to the magnetic properties of Co, all calculations were spin-polarized

with an energy cutoff of 380 eV. The Brillouin zone was sampled by a $2 \times 2 \times 1$ k-points grid generated via the Monkhorst-Pack procedure [33]. The geometry optimization was converged when the energy differences between two electronic optimization steps were smaller than 10^{-5} eV, and the forces for ions were less than 0.05 eV/Å. For the transition state (TS) search calculations of all elementary reactions in HCHO oxidation process, the complete LST/QST was adopted for search protocol, and the convergence tolerance of RMS convergence resorted to 0.25 eV/Å. In order to further confirm that the transition from reactant to product went through a transition state structure, the obtained transition state from TS search will be further checked via TS confirmation. The output of a TS confirmation calculation is another trajectory document, which follows the Intrinsic Reaction Path (IRP) as discussed in reaction paths.

The adsorption energy of all reactants, intermediates, and product species can be calculated through the following formula:

$$E_{\text{ads}} = E_{\text{species/slab}} - E_{\text{species}} - E_{\text{slab}} \quad (1)$$

where $E_{\text{species/slab}}$ represents the total energy of Co_3O_4 (110) surface adsorbing certain species, E_{species} represents the energy of sole species, E_{slab} represents the slab energy of Co_3O_4 (110) surface.

Based on the calculation results, all the adsorption energies are negative. Therefore, we take absolute values to compare the adsorption energies of different surface species.

The desorption time (τ) was calculated through the following formula:

$$\tau = \frac{1}{Ae^{\frac{E_{\text{des}}}{k_B T}}} \quad (2)$$

where A is bond vibration frequency in the range of 1012 Hz, k_B is the Boltzmann constant (8.63×10^{-5} eV/K) and T is the room temperature of 298.15 K. E_{des} is the desorption energy.

For a reaction such as R (reactant) \rightarrow P (product) on catalyst surface, the activation barrier (E_a) and reaction energy (ΔE) were calculated according to the following formulas:

$$E_a = E_{\text{TS}} - E_R \quad (3)$$

$$\Delta E = E_P - E_R \quad (4)$$

Where E_R and E_P are the total energies of the adsorbed reactant and product, respectively, and E_{TS} represent the total energies of the transition state.

The energetic span (δE) model was also employed to elucidate the efficiency of the catalytic cycles. According to the literature, there were only two states to determine δE , namely determining transition state (DTS) and determining intermediate state (DIS), the smaller the energy span, the faster the reaction. δE is shown as:

$$\delta E = \begin{cases} T_{\text{TDTS}} - I_{\text{TDI}}, & \text{if TDTS appears after TDI (a)} \\ T_{\text{TDTS}} - I_{\text{TDI}} + \Delta E_r, & \text{if TDTS appears before TDI (b)} \end{cases} \quad (5)$$

4. Conclusions

DFT calculations have been performed to investigate possible HCHO catalytic oxidation paths on pristine Co_3O_4 (110) surface for comparisons of different reaction mechanisms. In addition, the maximum δE is calculated to state the catalytic cycle. The following results were obtained. HCHO and O_2 prefer to co-adsorb on the Co_3O_4 (110) surface. The transfer of the H atom of HCHO to O_2 for HCO and OOH formation represents the first preferable step rather than O_2 dissociation. The electron property of PDOS analysis further suggests that only the α π^* orbitals of O_2 are partially occupied, forcing O_2 to be of a radical nature, which is active for hydrogenation. HCO is further prone to transfer its H atom to OOH to generate CO and HOOH. Regarding the MvK mechanism, through CO grabbing O_{latt} , CO_2 is produced and the O vacancy is filled by one OH group originating from HOOH

bond breakage. Meanwhile, the H atom approaches in close proximity to OH to form H₂O. For the L-H mechanism, CO obtains one OH from HOOH, then COOH gives an H atom to another OH for the formation of CO₂ and H₂O. Comparing the maximum activation barrier and δE , both the MvK and L-H mechanism are found to be feasible. Lattice oxygen in the MvK mechanism and surface OH in the L-H mechanism are both key ROS for oxidation of CO intermediates, and the catalytic cycle is almost equivalent.

Author Contributions: Conceptualization, Y.H., R.L. and T.H.; methodology, R.L. and T.H.; software, R.L. and T.H.; validation, R.L. and T.H.; formal analysis, R.L. and T.H.; data curation, R.L.; writing—original draft preparation, R.L. and T.H.; writing—R.L.; visualization, T.H.; supervision, Y.H., M.C. and W.H.; project administration, S.-c.L. and J.C.; funding acquisition, Y.H. All authors have read and agreed to the published version of the manuscript.

Funding: This work was funded by National Science Foundation of China, China [grant Nos. 51878644 and 41573138], the Strategic Priority Research Program of the Chinese Academy of Sciences, China [grant Nos. XDA23010300 and XDA23010000], the National Key Research and Development Program of China, China [grant No. 2016YFA0203000], and the Plan for “National Youth Talents” of the Organization Department of the Central Committee.

Data Availability Statement: Not applicable.

Conflicts of Interest: The authors declare no conflict of interest.

References

1. Salthammer, T.; Mentese, S.; Marutzky, R. Formaldehyde in the Indoor Environment. *Chem. Rev.* **2010**, *110*, 2536–2572. [[CrossRef](#)]
2. Huang, Y.; Ho, S.S.H.; Ho, K.F.; Lee, S.C.; Yu, J.Z.; Louie, P.K.K. Characteristics and health impacts of VOCs and carbonyls associated with residential cooking activities in Hong Kong. *J. Hazard. Mater.* **2011**, *186*, 344–351. [[CrossRef](#)] [[PubMed](#)]
3. Nie, L.; Yu, J.; Jaroniec, M.; Tao, F.F. Room-temperature catalytic oxidation of formaldehyde on catalysts. *Catal. Sci. Technol.* **2016**, *6*, 3649–3669. [[CrossRef](#)]
4. Wang, J.; Li, J.; Jiang, C.; Zhou, P.; Zhang, P.; Yu, J. The effect of manganese vacancy in birnessite-type MnO₂ on room-temperature oxidation of formaldehyde in air. *Appl. Catal. B Environ.* **2017**, *204*, 147–155. [[CrossRef](#)]
5. Li, H.; Huang, T.; Lu, Y.; Cui, L.; Wang, Z.; Zhang, C.; Lee, S.; Huang, Y.; Cao, J.; Ho, W. Unraveling the mechanisms of room-temperature catalytic degradation of indoor formaldehyde and its biocompatibility on colloidal TiO₂-supported MnO_x-CeO₂. *Environ. Sci. Nano* **2018**, *5*, 1130–1139. [[CrossRef](#)]
6. Huang, Y.; Liu, Y.; Wang, W.; Chen, M.; Li, H.; Lee, S.-C.; Ho, W.; Huang, T.; Cao, J. Oxygen vacancy-engineered δ -MnO_x/activated carbon for room-temperature catalytic oxidation of formaldehyde. *Appl. Catal. B Environ.* **2020**, *278*, 119294. [[CrossRef](#)]
7. Zhu, D.; Chen, M.; Huang, Y.; Li, R.; Huang, T.; Cao, J.-j.; Shen, Z.; Lee, S.C. FeCo alloy encased in nitrogen-doped carbon for efficient formaldehyde removal: Preparation, electronic structure, and d-band center tailoring. *J. Hazard. Mater.* **2022**, *424*, 127593. [[CrossRef](#)]
8. Zhang, C.; He, H.; Tanaka, K.-I. Catalytic performance and mechanism of a Pt/TiO₂ catalyst for the oxidation of formaldehyde at room temperature. *Appl. Catal. B Environ.* **2006**, *65*, 37–43. [[CrossRef](#)]
9. Jabłońska, M.; Król, A.; Kukulska-Zajac, E.; Tarach, K.; Girman, V.; Chmielarz, L.; Góra-Marek, K. Zeolites Y modified with palladium as effective catalysts for low-temperature methanol incineration. *Appl. Catal. B Environ.* **2015**, *166–167*, 353–365. [[CrossRef](#)]
10. Chen, B.-B.; Zhu, X.-B.; Crocker, M.; Wang, Y.; Shi, C. FeO_x-supported gold catalysts for catalytic removal of formaldehyde at room temperature. *Appl. Catal. B Environ.* **2014**, *154–155*, 73–81. [[CrossRef](#)]
11. Bai, B.; Li, J. Positive Effects of K⁺ Ions on Three-Dimensional Mesoporous Ag/Co₃O₄ Catalyst for HCHO Oxidation. *ACS Catal.* **2014**, *4*, 2753–2762. [[CrossRef](#)]
12. Bai, B.; Arandiyán, H.; Li, J. Comparison of the performance for oxidation of formaldehyde on nano-Co₃O₄, 2D-Co₃O₄, and 3D-Co₃O₄ catalysts. *Appl. Catal. B Environ.* **2013**, *142–143*, 677–683. [[CrossRef](#)]
13. Huang, Y.; Long, B.; Tang, M.; Rui, Z.; Balogun, M.-S.; Tong, Y.; Ji, H. Bifunctional catalytic material: An ultrastable and high-performance surface defect CeO₂ nanosheets for formaldehyde thermal oxidation and photocatalytic oxidation. *Appl. Catal. B Environ.* **2016**, *181*, 779–787. [[CrossRef](#)]
14. Zeng, L.; Song, W.; Li, M.; Zeng, D.; Xie, C. Catalytic oxidation of formaldehyde on surface of HTiO₂/HCTiO₂ without light illumination at room temperature. *Appl. Catal. B Environ.* **2014**, *147*, 490–498. [[CrossRef](#)]
15. Li, H.; Ho, W.; Cao, J.; Park, D.; Lee, S.-C.; Huang, Y. Active Complexes on Engineered Crystal Facets of MnO_x-CeO₂ and Scale-Up Demonstration on an Air Cleaner for Indoor Formaldehyde Removal. *Environ. Sci. Technol.* **2019**, *53*, 10906–10916. [[CrossRef](#)] [[PubMed](#)]

16. Li, H.; Cui, L.; Lu, Y.; Huang, Y.; Cao, J.; Park, D.; Lee, S.-C.; Ho, W. In Situ Intermediates Determination and Cytotoxicological Assessment in Catalytic Oxidation of Formaldehyde: Implications for Catalyst Design and Selectivity Enhancement under Ambient Conditions. *Environ. Sci. Technol.* **2019**, *53*, 5230–5240. [[CrossRef](#)] [[PubMed](#)]
17. Li, R.; Huang, Y.; Zhu, D.; Ho, W.; Cao, J.; Lee, S. Improved Oxygen Activation over a Carbon/Co₃O₄ Nanocomposite for Efficient Catalytic Oxidation of Formaldehyde at Room Temperature. *Environ. Sci. Technol.* **2021**, *55*, 4054–4063. [[CrossRef](#)] [[PubMed](#)]
18. Li, R.; Huang, Y.; Zhu, D.; Ho, W.; Lee, S.; Cao, J. A Review of Co₃O₄-based Catalysts for Formaldehyde Oxidation at Low Temperature: Effect Parameters and Reaction Mechanism. *Aerosol Sci. Eng.* **2020**, *4*, 147–168. [[CrossRef](#)]
19. Ma, C.; Wang, D.; Xue, W.; Dou, B.; Wang, H.; Hao, Z. Investigation of Formaldehyde Oxidation over Co₃O₄–CeO₂ and Au/Co₃O₄–CeO₂ Catalysts at Room Temperature: Effective Removal and Determination of Reaction Mechanism. *Environ. Sci. Technol.* **2011**, *45*, 3628–3634. [[CrossRef](#)]
20. Wang, Z.; Wang, W.; Zhang, L.; Jiang, D. Surface oxygen vacancies on Co₃O₄ mediated catalytic formaldehyde oxidation at room temperature. *Catal. Sci. Technol.* **2016**, *6*, 3845–3853. [[CrossRef](#)]
21. Yan, Z.; Xu, Z.; Cheng, B.; Jiang, C. Co₃O₄ nanorod-supported Pt with enhanced performance for catalytic HCHO oxidation at room temperature. *Appl. Surf. Sci.* **2017**, *404*, 426–434. [[CrossRef](#)]
22. Zha, K.; Sun, W.; Huang, Z.; Xu, H.; Shen, W. Insights into High-Performance Monolith Catalysts of Co₃O₄ Nanowires Grown on Nickel Foam with Abundant Oxygen Vacancies for Formaldehyde Oxidation. *ACS Catal.* **2020**, *10*, 12127–12138. [[CrossRef](#)]
23. Cai, Y.; Xu, J.; Guo, Y.; Liu, J. Ultrathin, Polycrystalline, Two-Dimensional Co₃O₄ for Low-Temperature CO Oxidation. *ACS Catal.* **2019**, *9*, 2558–2567. [[CrossRef](#)]
24. Bae, J.; Shin, D.; Jeong, H.; Choe, C.; Choi, Y.; Han, J.W.; Lee, H. Facet-Dependent Mn Doping on Shaped Co₃O₄ Crystals for Catalytic Oxidation. *ACS Catal.* **2021**, *11*, 11066–11074. [[CrossRef](#)]
25. Xiao, M.; Yu, X.; Guo, Y.; Ge, M. Boosting Toluene Combustion by Tuning Electronic Metal–Support Interactions in In Situ Grown Pt@Co₃O₄ Catalysts. *Environ. Sci. Technol.* **2022**, *56*, 1376–1385. [[CrossRef](#)]
26. Deng, J.; Song, W.; Chen, L.; Wang, L.; Jing, M.; Ren, Y.; Zhao, Z.; Liu, J. The effect of oxygen vacancies and water on HCHO catalytic oxidation over Co₃O₄ catalyst: A combination of density functional theory and microkinetic study. *Chem. Eng. J.* **2019**, *355*, 540–550. [[CrossRef](#)]
27. Wang, X.; Ying, J.; Mai, Y.; Zhang, J.; Chen, J.; Wen, M.; Yu, L. MOF-derived metal oxide composite Mn₂Co₁O_x/CN for efficient formaldehyde oxidation at low temperature. *Catal. Sci. Technol.* **2019**, *9*, 5845–5854. [[CrossRef](#)]
28. Chen, J.; Huang, M.; Chen, W.; Tang, H.; Jiao, Y.; Zhang, J.; Wang, G.; Wang, R. Defect Engineering and Synergistic Effect in Co₃O₄ Catalysts for Efficient Removal of Formaldehyde at Room Temperature. *Ind. Eng. Chem. Res.* **2020**, *59*, 18781–18789. [[CrossRef](#)]
29. Wang, N.; Xu, Z.; Luo, T.; Yan, Z.; Jin, M.; Shi, L. Pt Anchored on Mn(Co)CO₃/MnCo₂O₄ Heterostructure for Complete Oxidation of Formaldehyde at Room Temperature. *ChemistrySelect* **2020**, *5*, 10537–10548. [[CrossRef](#)]
30. Jiang, Q.G.; Ao, Z.M.; Li, S.; Wen, Z. Density functional theory calculations on the CO catalytic oxidation on Al-embedded graphene. *RSC Adv.* **2014**, *4*, 20290–20296. [[CrossRef](#)]
31. Chen, J.; Selloni, A. Electronic states and magnetic structure at the Co₃O₄ (110) surface: A first-principles study. *Phys. Rev. B* **2012**, *85*, 085306. [[CrossRef](#)]
32. Perdew, J.P.; Chevary, J.A.; Vosko, S.H.; Jackson, K.A.; Pederson, M.R.; Singh, D.J.; Fiolhais, C. Atoms, molecules, solids, and surfaces: Applications of the generalized gradient approximation for exchange and correlation. *Phys. Rev. B* **1992**, *46*, 6671–6687. [[CrossRef](#)] [[PubMed](#)]
33. Pack, J.D.; Monkhorst, H.J. “Special points for Brillouin-zone integrations”—A reply. *Phys. Rev. B* **1977**, *16*, 1748–1749. [[CrossRef](#)]